Icarus **140**, 369–378 (1999)
Article ID icar.1999.6142, available online at http://www.idealibrary.com on IDEAL®

Physical Model of Asteroid 1620 Geographos from Radar and Optical Data

R. S. Hudson

School of Electrical Engineering and Computer Science, Washington State University, Pullman, Washington 99164-2752
E-mail: hudson@eecs.wsu.edu

and

S. J. Ostro

Jet Propulsion Laboratory, California Institute of Technology, Pasadena, California 91109-8099

Received October 1, 1998; revised March 19, 1999

We develop a physical model of asteroid 1620 Geographos using Goldstone delay–Doppler radar images obtained August 1994 (Ostro *et al.* 1996, *Icarus* 121, 46–66) with resolution as fine as 75 m, and optical lightcurves obtained in 1969, 1983, and 1993–1994 (Magnusson *et al.* 1996, *Icarus* 123, 227–244). The data set admits a geometric ambiguity that precludes a unique model. Within this constraint, our model has maximum dimensions of (5.0, 2.0, 2.1) $\pm$ 0.15 km and a volume of $\leq$8.8 km^3, equivalent to a sphere of $\leq$2.56 km diameter. The radar equivalent spherical albedo is $\geq$0.12. The photometric solution provides Hapke parameters $w \geq 0.22$, $g = -0.34 \pm 0.10$, and $\bar{\theta} = 25 \pm 10^\circ$ with assumed values $h = 0.02$ and $B_0 = 1.32$. The spin state solution does not differ significantly from that of Magnusson *et al.* having $\lambda = 55 \pm 6^\circ$, $\beta = -46 \pm 4^\circ$, and $P = 5.2233270 \pm 0.00000072$ h. We identify seven main features in the delay–Doppler images and their corresponding locations on the model.

Key Words: **asteroids; radar; photometry; image processing.**

INTRODUCTION

The Earth-crossing asteroid (ECA) 1620 Geographos is interesting on several accounts. It is on the Minor Planet Center's list of Potentially Hazardous Asteroids (on the World Wide Web at http://cfa-www.harvard.edu/iau/lists/Dangerous.html). At about 5 km in maximum dimension, it is one of the larger of such objects. Lightcurves obtained in 1969 showed an amplitude of more than 2 magnitudes indicating a very elongated object (Magnusson *et al.* 1996). Radar observations during 1994 allowed unambiguous determination of the asteroid's pole-on silhouette and established it as the most elongated Solar System object imaged to date (Ostro *et al.* 1995). Geographos was to have been the final target of the Clementine I spacecraft, which would have made it the first ECA to be so visited. Unfortunately Clementine was unable to undertake that phase of its mission. So we are left with groundbased data to characterize this asteroid. In this paper we use the existing optical and radar data to form a physical model of Geographos.

The construction of a physical model from radar data has been demonstrated for the ECAs 4769 Castalia (Hudson and Ostro 1994) and 4179 Toutatis (Hudson and Ostro 1995). The models have been used to understand the asteroid's lightcurves, a process that also provided an independent test of the validity of the radar-derived models (Hudson *et al.* 1997, Hudson and Ostro 1998). As discussed below, with respect to physical modeling the Geographos radar data set has a geometric ambiguity not present in these other ECA radar data sets. In order to gain the maximum possible leverage over the shape, we have incorporated the optical data directly into the modeling process from the start.

DATA SET

The optical data set (Magnusson *et al.* 1996) used in this paper consists of 93 lightcurves. The great majority were taken during 1993–1994, but seven were from 1969 and two were from 1983. Solar phase angles ranged from 10.9° to 60.5°. Of these we judged 30 to provide reliable absolute V-filter photometry while for the remainder we allowed a calibration offset. The total number of optical data used was 5208.

The long time base of the optical data set allows for precise calculation of the sidereal spin period P. Magnusson *et al.* (1996) applied various techniques to determine P, the pole direction and an ellipsoidal shape model. They found $P = 5.22332640$ h and pole direction $\lambda = 56^\circ$, $\beta = -47^\circ$. They modeled the shape of Geographos as a biaxial ellipsoid with elongation 2.58. They also investigated possible perturbations of the model that could account for the unequal lightcurve extrema.

The radar data set (Ostro *et al.* 1996) was collected at Goldstone between August 28 and September 2, 1994. The

0019-1035/99 $30.00

highest resolution imaging was conducted on August 30 and 31 and achieved resolutions of 75 m in delay and 87 m in Doppler. Pole solutions from the optical data suggested that the radar would stay very close to the asteroid's equator throughout the entire experiment. The radar images verified this geometry as the image sequence was essentially unchanged from day to day in spite of considerable plane of sky motion between dates. Because of this redundancy and the fact that the August 30 data had a higher signal-to-noise ratio, we have used only the August 30 data in our modeling.

DELAY–DOPPLER IMAGING

Because the delay–Doppler imaging geometry is essential to understanding the limitations of the Geographos data set, we here give a brief overview of it. With reference to Fig. 1, the (x, y, z) "body coordinates" are fixed on the asteroid with the z axis corresponding to the spin vector. The (x_r, y_r, z_r) "radar coordinates" are oriented such that the radar lies on the x_r axis and the z_r axis is the projection of the spin vector on the plane of sky.

The radar looks down the x_r axis and sees something like that shown in Fig. 2. Contours of constant delay (constant x_r) are analogous to elevation contours on a topographic map. Iso-Doppler contours are lines parallel to the projected spin vector (constant y_r). Intersections between an iso-delay and iso-Doppler contour define a delay–Doppler resolution cell. It is often the case that these contours will intersect at two or more different points. Echo power from all these points will contribute to the corresponding pixel in a delay–Doppler image. This many-to-one mapping is referred to as the "north–south ambiguity" (NSA), and it complicates the interpretation of delay–Doppler images.

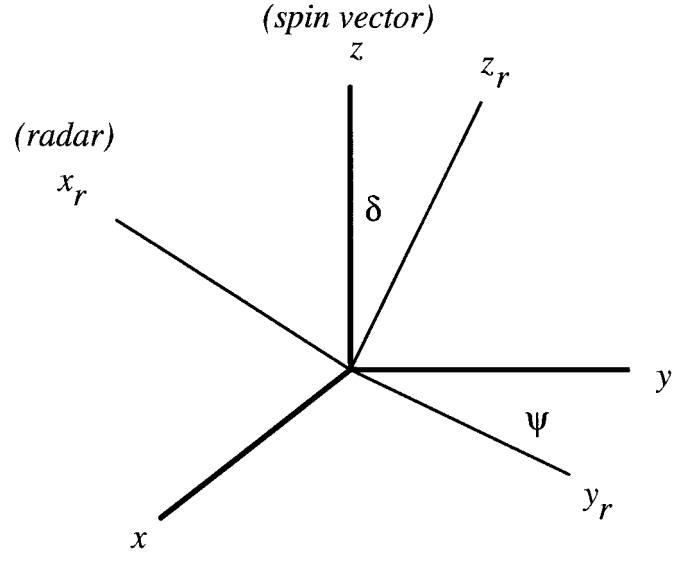

FIG. 1. Relation between asteroid and radar coordinates. Angles δ and ψ are the subradar latitude and rotation phase, respectively.

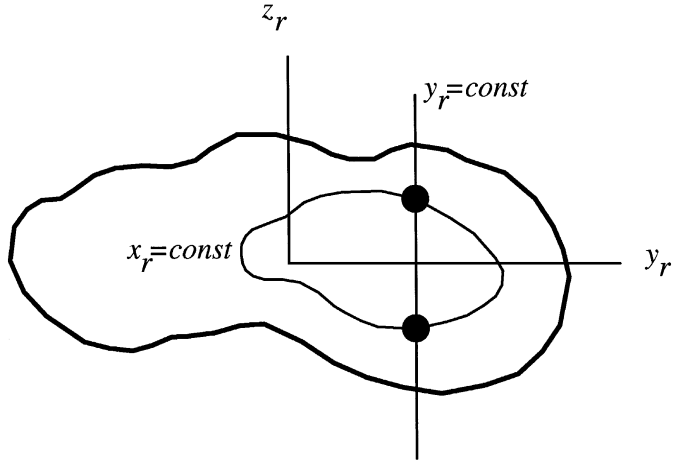

FIG. 2. Plane of sky appearance of asteroid and iso-delay ($x_r = \text{const}$) and iso-Doppler ($y_r = \text{const}$) contours.

Given sufficient geometric diversity it is often possible to resolve the NSA with a sequence of images. The radar and asteroid coordinates are related by

$$x_r = (x \cos\psi - y \sin\psi)\cos\delta + z \sin\delta$$
$$y_r = x \sin\psi + y \cos\psi$$
$$z_r = -(x \cos\psi - y \sin\psi) + z \cos\delta,$$

where δ is the subradar latitude and ψ is the rotation phase. If $\delta \neq 0$ there is a one-to-one relation between a given point (x, y, z) and its delay–Doppler trajectory; that is, no other point has the same values of x_r and y_r as ψ varies over some interval. Two points that are ambiguous in one image will not be ambiguous in subsequent images. A rough analogy can be made between a delay–Doppler image sequence and a set of linearly independent equations. Although the value of an individual unknown cannot be determined from any single equation, the leverage afforded by the complete set of equations lets one find a unique solution for all unknowns.

However, the uniqueness of delay–Doppler trajectories breaks down when $\delta = 0$, because any points with the same x and y values will always have the same x_r and y_r values and consequently always fall into the same delay–Doppler pixel. This is analogous to having a set of equations that are linearly dependent; it is no longer possible to solve uniquely for each unknown. During the Geographos radar experiment the asteroid's pole was oriented essentially perpendicular to the object's motion on the sky. So, even though the asteroid moved several tens of degrees on the sky, δ remained essentially zero throughout the experiment.

Note that even when delay–Doppler trajectories are not unique, the delay–Doppler images still contain photometric information about the slopes of surface facets. However, this differential shape information available from image shading is not as strong as the purely geometric leverage resulting from unique delay–Doppler trajectories.

To explore the effects of an equatorial view on radar-based shape reconstruction, we used a laser radar system (Andrews *et al.* 1995) to produce laser "delay–Doppler" images of a scale model clay "asteroid" with $\delta = 0$ geometry. The fractional resolution and signal-to-noise of the laboratory images were set to be similar to the Geographos radar data set. A physical model was produced from this laboratory data in the same manner as used to develop the Geographos model described below. Comparison of this model with the known shape serves as a type of "calibration" for the Geographos results and can give us an idea of the types of distortions that might be present in the Geographos model.

Figure 3 shows "observed" and modeled laser "delay–Doppler" images. The model has accounted for the appearance of the delay–Doppler image, but, as Fig. 4 shows, this does not mean that the shapes of the clay model and the computer reconstruction are as close. In fact, to a considerable extent, the reconstruction has "symmetrized" the actual shape along the spin vector (up/down) direction. Features in the model, such as bends and concavities, correspond to real features on the object, but are typically distorted and/or distributed ambiguously between north and south.

We see that a reconstruction in the $\delta = 0$ case can give us an indication of the presence and type of surface features, but cannot constrain their morphology or north/south (N/S) location(s) uniquely. It is also clear that if the actual shape is not N/S symmetric, then the symmetrization of the model will tend to lead to an overestimation of the extents along the spin vector direction and consequently also the volume and surface area. Given that our modeling also treats the radar and photometric properties as free parameters, this most likely will lead to a systematic underestimation of albedo.

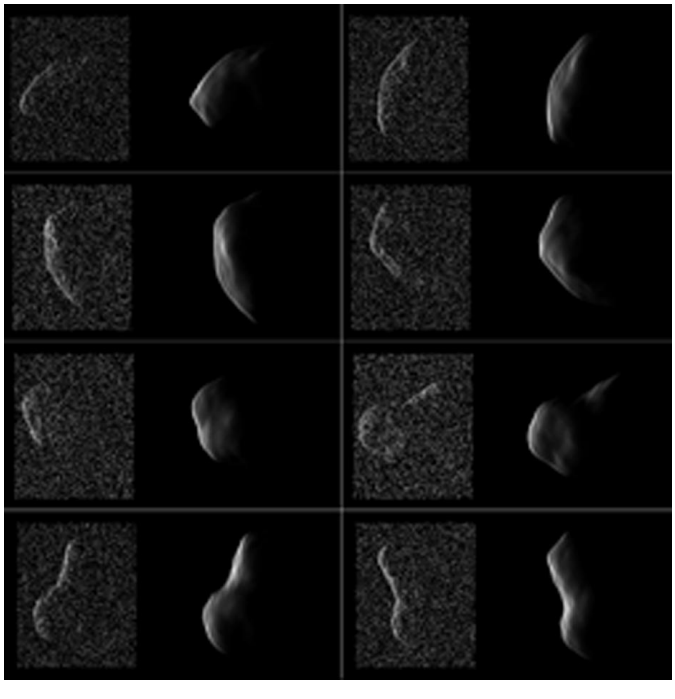

FIG. 3. Observed (first and third columns) and modeled (second and fourth columns) laser–radar images of clay model asteroid. Fractional resolution and signal-to-noise ratio is similar to Goldstone Geographos radar data set.

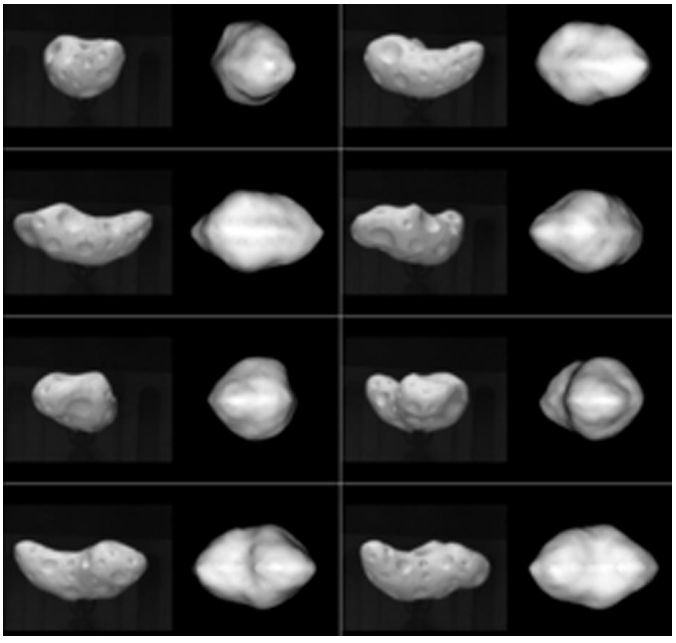

FIG. 4. True shape (first and third columns) and modeled shape (second and fourth columns) of clay asteroid model. Spin vector is up.

MODELING

Our physical model of Geographos parameterizes shape, photometric properties (both optical and radar), and spin state. The shape is described by a collection of 1020 triangular facets defined by the locations of 512 vertices. Vertex locations were defined with respect to a point on a reference ellipsoid and were free to move in the direction of the ellipsoid's surface normal at the reference point. Consequently the model represents a deformed ellipsoid. We arrived at the final number of facets by adding vertices during the modeling process until further additions did not lead to a significantly improved fit.

The optical properties of the surface were modeled using a homogeneous, five parameter Hapke photometric function with a single-parameter Henyey–Greenstein particle phase function (Hapke 1993, Eq. 12.55), as was used to model lightcurves of Gaspra (Simonelli *et al.* 1995), Ida (Simonelli *et al.* 1996), Castalia (Hudson *et al.* 1997), and Toutatis (Hudson and Ostro 1998). The solar phase angle in the optical data set never went below 10°, and the fits displayed little sensitivity to the opposition surge parameters h and B_0, so we fixed these at the "average S-class asteroid" values of $h = 0.02$, $B_0 = 1.32$ (Helfenstein *et al.* 1996).

Our model radar scattering function has the form $\rho \cos^n \phi$. Here ϕ is the angle of incidence, ρ is the normal reflectivity

(related to albedo), and n is a measure of the angular width of the scattering pattern. Typically a large value of n corresponds to a surface that is smooth at the scale of an image resolution cell while a small value of n corresponds to a rough surface. (A Lambertian surface has $n = 2$.)

Tentatively, the spin state was assumed to be that of a uniform-density body in principal axis rotation about the axis of maximum moment of inertia. We enforced this by introducing a term into the goodness-of-fit measure that penalized any inconsistencies between the shape and this assumption. We were prepared to relax this constraint and admit a non-principal-axis spin state and/or density inhomogeneities if our original assumption was not supported by the data. We used the spin state of Magnusson *et al.* (1996) for our initial conditions.

As the optical data set has a much longer time base than the radar data set, it provides the most leverage for estimating the spin state. Hence, we began modeling by fitting a biaxial ellipsoid to the optical data and solving for the axes, the spin state, and Hapke parameters. Then we approximated that ellipsoid with a triangular-facet polyhedron. Because we were interested to see the extent to which the optical data could resolve the NSA, we used the following procedure. We froze the spin state and fit the shape to the radar data alone. At this point the optical data were included in the modeling, allowing us to see the changes required to the model by the addition of those data. These changes were observable although not very great. Given the probability that the radar-only model suffered from the types of distortions evident in the laboratory experiment, this implies that the optical data did not provide a great deal of leverage to resolve the NSA. Indeed, the sub-Earth latitudes sampled by the lightcurves never extend far into the north or south, but remain within a few tens of degrees of the equator. Nonetheless, as discussed below, there is evidence that the complete data set has some sensitivity to the N/S position of surface features.

Figure 5 shows the observed and modeled radar data corresponding to August 30. Figure 6 shows six of the 93 lightcurve fits. (Plots for all 93 lightcurves are available at http://www.eecs.wsu.edu/~hudson/asteroids.html) The top three lightcurves represent a few extremes. The 1969 lightcurve has one of the most northerly sub-Earth latitudes at about 20° and one of the larger phase angles at 53°. The 1983 curve has the smallest phase angle at 11°. The 1994-3-11 curve has one of the more southerly subearth latitudes at $-27°$ and a large phase angle of 50°. The bottom three lightcurves are somewhat representative of the rest of the data set. Generally the model accounts for the asymmetric lightcurve minima but there are cases in which it fails to, as in the 1993-12-13 curve where the deepest observed minimum is about 0.2 mag lower than the modeled minimum. The total rms residual for the entire optical data set was 0.08 magnitude.

Figures 7 and 8 show the shape model. Lines of constant latitude and longitude are drawn at 10° intervals. The views in Fig. 7 are from above the north and south poles, while those of Fig. 8 are from within the equatorial plane.

RESULTS

Our model "explains" the observed radar and optical data using a fairly detailed shape model and realistic photometric functions and rotational dynamics. It follows that the model *could be* an accurate representation of Geographos. However, as shown above, there are geometric ambiguities in the data set that probably result in distortion and symmetrization of the shape along the direction of the spin vector. Nonetheless, with the currently available data this model is probably the farthest we can go toward determining the physical properties of Geographos. Consequently we will take it at face value and discuss its implications, keeping in mind that features appearing in the model arise from real features on the object.

Shape

Resolution of the model along directions parallel to the equatorial plane is determined by the ~75-m resolution of the radar images. We conservatively adopt an uncertainty of two pixels or 0.15 km. As illustrated in Fig. 4 the NSA quite likely introduces a large and unknown systematic error for the orthogonal dimension. Keeping this in mind, we adopt 0.15 km as a general uncertainty for distance measurements.

Our shape model has maximum dimensions along the (long, intermediate, short) axes of inertia of $(5.0, 2.0, 2.1) \pm 0.15$ km. The corresponding moments of inertia are $(1.0, 3.7, 3.7) \pm 0.3$. The volume is 8.8 ± 1.6 km^3, equivalent to a sphere of diameter 2.56 km. A homogeneous ellipsoid with the same volume and moments of inertia would have extents of (4.7, 1.9, 1.9) km, i.e., a biaxial ellipsoid. Of course in this case there is no real distinction between intermediate and short axes. Given the possibility of symmetrization along the spin axis, the true inertia ellipsoid may be triaxial. Note that there is no inconsistency between the model's biaxial inertia ellipsoid and the shape's different maximum dimensions along the short and intermediate axes. The inertia tensor is determined by integrals over the shape's distribution of volume while the maximum dimensions are directly effected by small features such as bumps at the extremities.

The most prominent large-scale feature is the bend near 90°E longitude. This clearly appears in the delay–Doppler images and was discussed by Ostro *et al.* (1996). Here, in the context of the three-dimensional model we are able to see how this feature explains the different lightcurve minima observed. In Fig. 9 we show the appearance of the model under solar illumination corresponding to the lightcurve extrema M1, m1, M2, m2 of the 1969-8-30 lightcurve (Fig. 6).

The "contact-binary" hypothesis is sometimes offered as an explanation for highly elongated shapes. Because of this, the distribution of mass along the long axis is of interest. Figure 10 plots the cross-sectional area normal to the long axis (x axis) as a function of position on that axis. If the density is uniform (as our model assumes) then this is also the mass distribution. There is no bifurcation of mass apparent in this plot. Consequently this result provides no evidence for, although it does not rule out, the

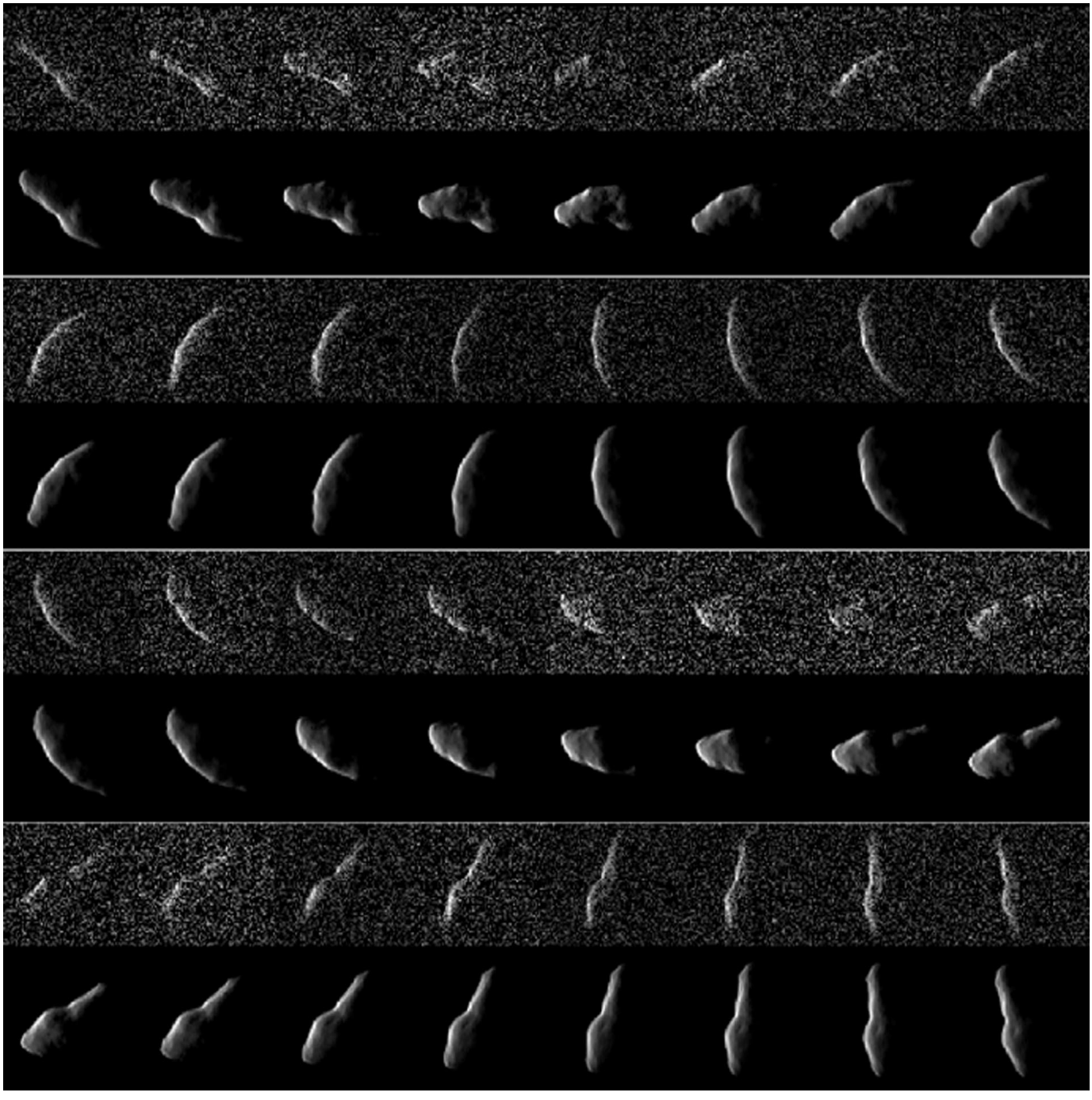

FIG. 5. Geographos delay–Doppler radar images. In each of the four sections the top row shows observed data and the row below shows the corresponding modeled data. Time increases from left to right and top to bottom. Delay increases from top to bottom and Doppler from left to right.

possibility that Geographos is a contact-binary asteroid, that is, that Geographos formed from two bodies that once were separate. It is interesting to note the qualitative similarity between the pole-on silhouettes of the Geographos model (Fig. 7) and the Ida model of Thomas *et al.* (1996, see Figs. 2c, 2f). Thomas *et al.* concluded that although the shape and observed properties of Ida indicate a dichotomy, they do not conclusively support the hypothesis of a contact binary structure. Regardless of the interpretation, if the rough similarity between Geographos and Ida are not a coincidence, it might indicate similar formation processes or collisional histories for the two objects. If so this would be very interesting, given that volume of Ida is more than three orders of magnitude greater than that of Geographos, and the former is a Main Belt object while the later is an ECA.

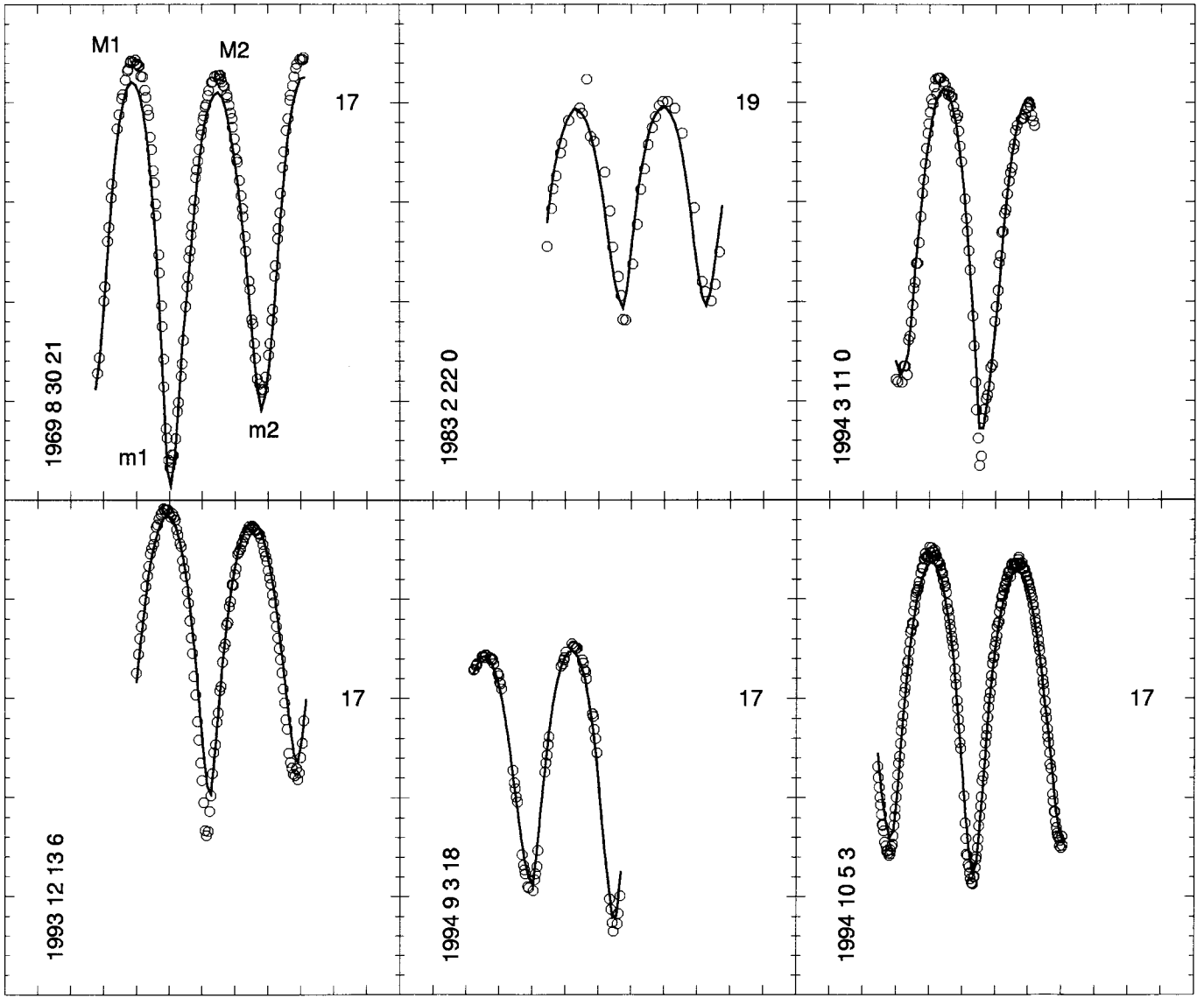

FIG. 6. Selected lightcurve fits. Vertical ticks are at 0.1 magnitude spacing. Horizontal ticks are at 1-h spacing. Vertical labels give UTC (year mn dd hh) at start of plot. Five of the lightcurves provided absolute photometry and one of the vertical ticks is labeled as a reference (V-filter magnitude corrected to 1 AU distances of either 17 or 19) while the other (top right) gives relative photometry only.

Surface Features

We identify seven surface features prominent in the delay–Doppler images, which we label C1–7 (Fig. 11), and discuss them in turn. The model is generated with respect to the rectangular body system (x, y, z) with origin at the center of mass. The z axis is the north pole while the x axis is the axis of minimum inertia pointing more or less in the direction of the 0° rotation phase origin adopted by Ostro *et al.* (1995). In this paper we will find it convenient to locate points on the surface by latitude (δ) and longitude (α). In Figs. 7, 8, and 11 longitude, latitude grids with 10° spacing have been drawn on the model to aid in this discussion. We define latitude (δ) and East longitude (α) by

$$r = \sqrt{x^2 + y^2 + z^2}$$

$$(x, y, z) = r(\sin\delta\cos\alpha, \sin\delta\sin\alpha, \cos\delta),$$

while west longitude is given by $360^\circ - \alpha$.

In Fig. 11 the seven features are circled. The middle panel shows delay–Doppler images summed over 30° rotation-phase windows, and it corresponds to Fig. 11c of Ostro *et al.* (1996). Viewing the shape model from above the north/south pole generated the top/bottom panel. The light source was in the equatorial plane and rotated 30° between images. For the top panel the

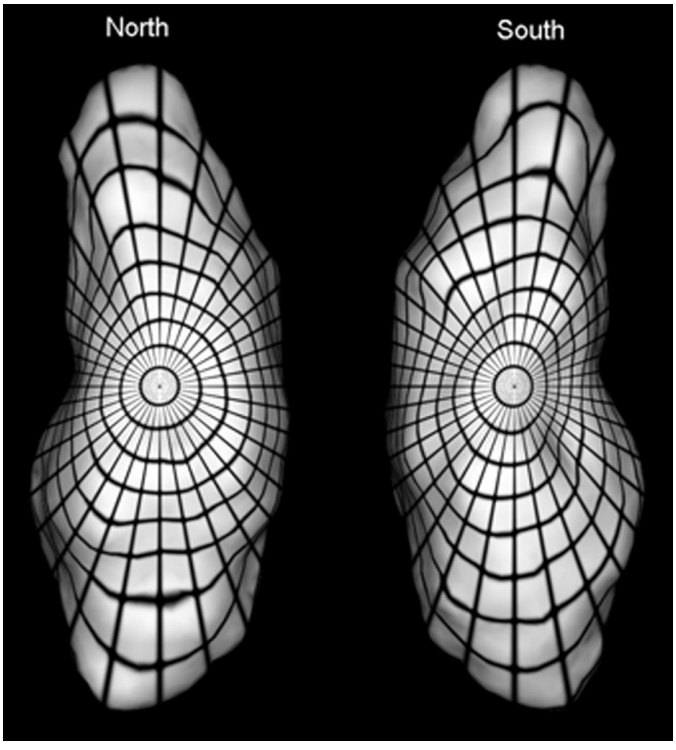

FIG. 7. View of the model from above north pole (left) and south pole (right). Contours of constant longitude and latitude are drawn at 10° intervals. 0° longitude is up.

images were flipped left to right to give them the same orientation as the south-pole orientation we have used to display the delay–Doppler images.

When viewed in this manner the appearance of the model is roughly analogous to a delay–Doppler image. However, there are some important differences that should not be forgotten. First, a delay–Doppler image combines the contributions from both the north and south. Second, the relation between surface normal and brightness is different for the two types of images. The model images are viewed at a 90° phase angle while the radar viewed the asteroid at 0° phase, so surface facets near the leading edge contribute significantly more energy to the delay–Doppler image than to the optical image. In short, *there is no optical imaging geometry that precisely corresponds to the delay–Doppler imaging geometry*. We have adjusted for this effect somewhat by applying a nonlinear brightness filter to the model images. Still, *it must not be assumed that the model when viewed in this manner is supposed to accurately predict the delay–Doppler images*. To do that, the correct delay–Doppler imaging geometry must be employed, as it is during the modeling process (Fig. 5). However, Fig. 11 does allow us to see what regions of the surface were unilluminated by the radar.

By viewing the model in this manner, we are able to see if it tends to place a feature in the north or south. For example, concavity features C1 and C2 are responsible for the "knobish," almost detached appearance of the 0° end. Figure 11 suggests that concavities located in the south are primarily responsible for these features. C1 is located near (5°S,10°W) while C2 is near (10°S,20°E).

Features C3, C4, and C5 are the features most suggestive of craters in the delay–Doppler images. The model prefers a southern location for C3 (40°S,20°W) and northern locations for C4 (90°N) and C5 (20°N,180°W).

C6 is the feature responsible for the pinwheel-like appearance of the 180°W end. The model places a concavity in the north at (10°N,170°E) to explain this.

C7 is an elongated feature that could possibly be two close craters. The model explains this by a concavity near (40°S,130°E).

Optical and Radar Scattering Properties

The radar scattering law has the form $\rho \cos^n \theta$, where ρ is normal reflectivity and n is a measure of the angular width of the scattering. If the surface scattering is modeled as specular reflection from a distribution of surface facets, then $\theta = \tan^{-1}\sqrt{2/n}$ is the rms surface slope and $R = 2\rho/(n+2)$ is the Fresnel reflection coefficient.

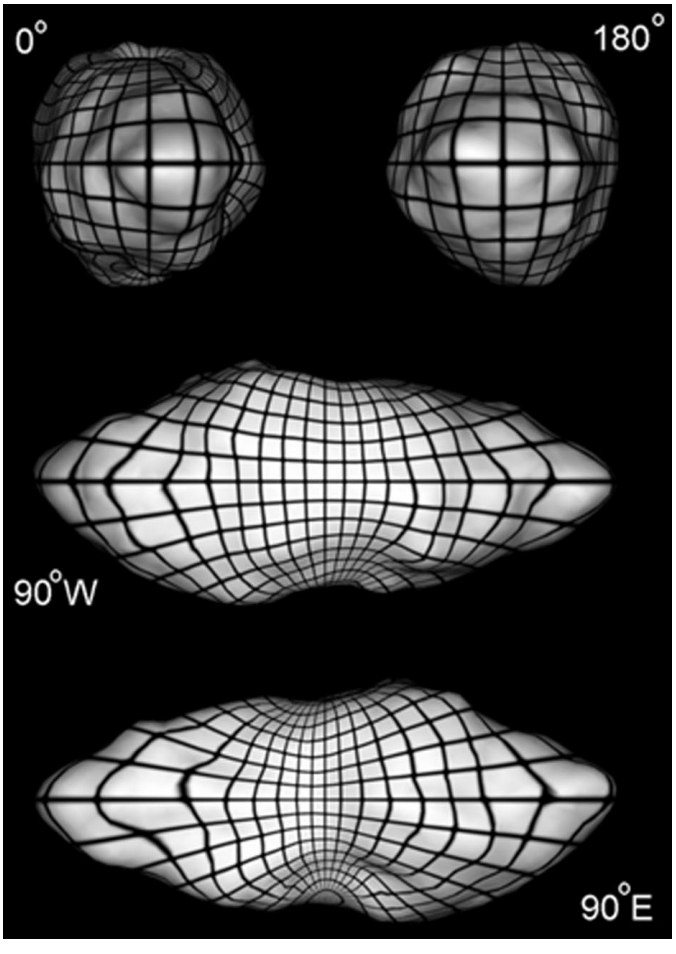

FIG. 8. Views of model from within equatorial plane. Central longitude of each view is indicated.

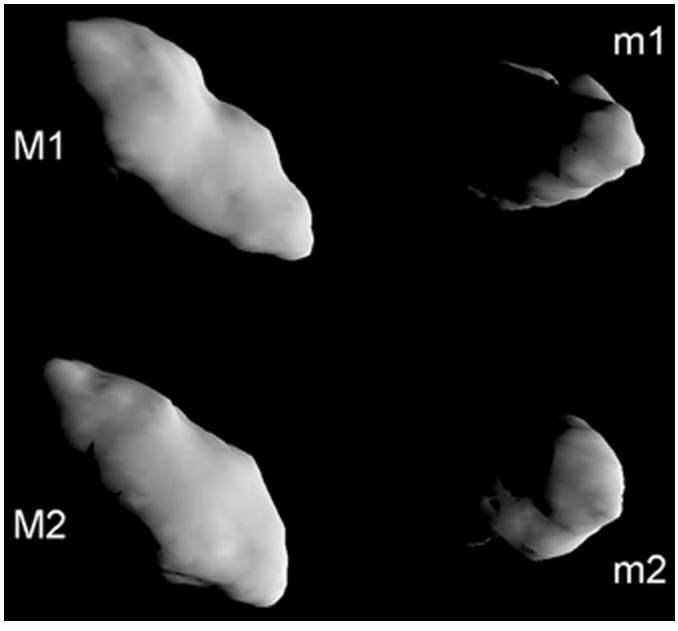

FIG. 9. Model viewed with solar illumination at times corresponding to extrema of 1969-8-30 lightcurve.

Our model gives $n = 1.72 \pm 0.5$ and $\rho \geq 0.17$ where we take the ρ solution as a lower bound in keeping with our assumption that the projected area of the model is likely to be larger than that of the asteroid. The value of n suggests more diffuse scattering than found for either Toutatis ($n = 2.3$) or Castalia ($n = 2.8$). The equivalent radar spherical albedo of Geographos is ≥ 0.12. For comparison Castalia's value is 0.16 and for Toutatis it is 0.21.

For the three Hapke parameters that we solved for, we found a single-scattering albedo $w \geq 0.22$, a Henyey–Greenstein asymmetry factor $g = -0.34 \pm 0.1$, and a macroscopic surface roughness $\bar{\theta} = 25 \pm 10^\circ$, where, in analogy with ρ, we take the model's w value as a lower bound. Uncertainties for g and $\bar{\theta}$ were derived through covariance calculations and a consideration of possible systematic errors due to the NSA. These values are quite close to those found for Dactyl, $w = 0.21$, $g = -0.33$, and $\bar{\theta} = 23^\circ$, for which opposition surge parameters $h = 0.02$ and $B_0 = 1.53$ were assumed (Helfenstein *et al.* 1996).

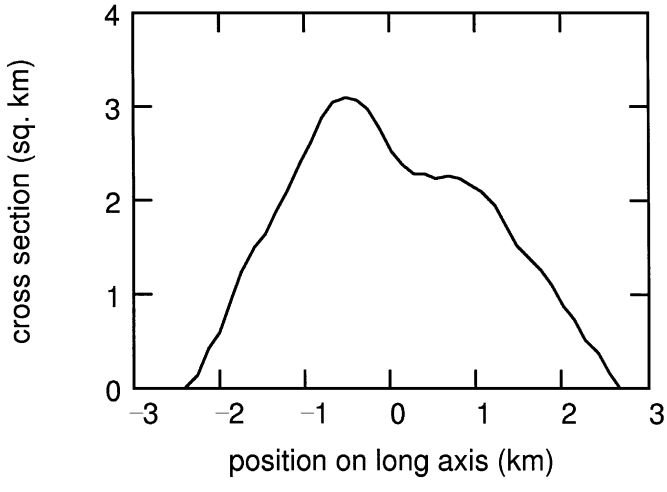

FIG. 10. Distribution of volume on long axis.

Spin State

Our spin state solution differs negligibly from that of Magnusson *et al.* (1996). This makes sense as we are using the same optical data and the optical data are what primarily constrain the spin state in this case. We found $\lambda = 55 \pm 6^\circ$, $\beta = -46 \pm 4^\circ$, and $P = 5.2233270 \pm 0.00000072$ h, where we have retained the uncertainties of Magnusson *et al.*

It has been suggested that subtle periodicities in the lightcurves provide evidence of non-principal-axis rotation and one or more companion satellites (Prokof'eva *et al.* 1997). We tested the non-principal-axis rotation hypothesis by freeing the spin state from the principal-axis, uniform-density constraints placed on it during most of the modeling. We observed no significant change in the fit and hence find no evidence for non-principal-axis rotation.

IMPLICATIONS

Our shape model is distinguished by its elongation, a major central indentation, circular concavities that most likely are impact craters with diameters of several hundred meters, other topographic relief that may or may not be impact craters, and unusual structure at the ends. How should these characteristics be understood? Ostro *et al.* (1996) surmised that "Geographos presumably is the cumulative product of a sequence of collisions, perhaps originating in disruption of a very much larger parent body and proceeding through an interval of relatively low-energy impacts." Richardson *et al.* (1998) have presented simulations that demonstrate the possibility that Geographos' shape has been resculpted by tidal distortion of a rubble pile during a close Earth encounter. Simulations by Scheeres *et al.* (1996, 1998) and Asphaug *et al.* (1998) demonstrate the complexity of the distribution of impact ejecta for small, irregularly shaped bodies and the dependence of the outcome of cratering events on the target's preexisting internal structure.

There probably are numerous, very different scenarios that could offer plausible qualitative explanations for this asteroid's detailed characteristics. For example, the unusual morphology of Geographos' ends may involve the systematics of ejecta removal and deposition caused by the combination of the asteroid's gravity field and rotation (Ostro *et al.* 1996), but other viable possibilities include tidal distortion, collisional spallation, and simply impact carving. Simulations using our model may elucidate these possibilities.

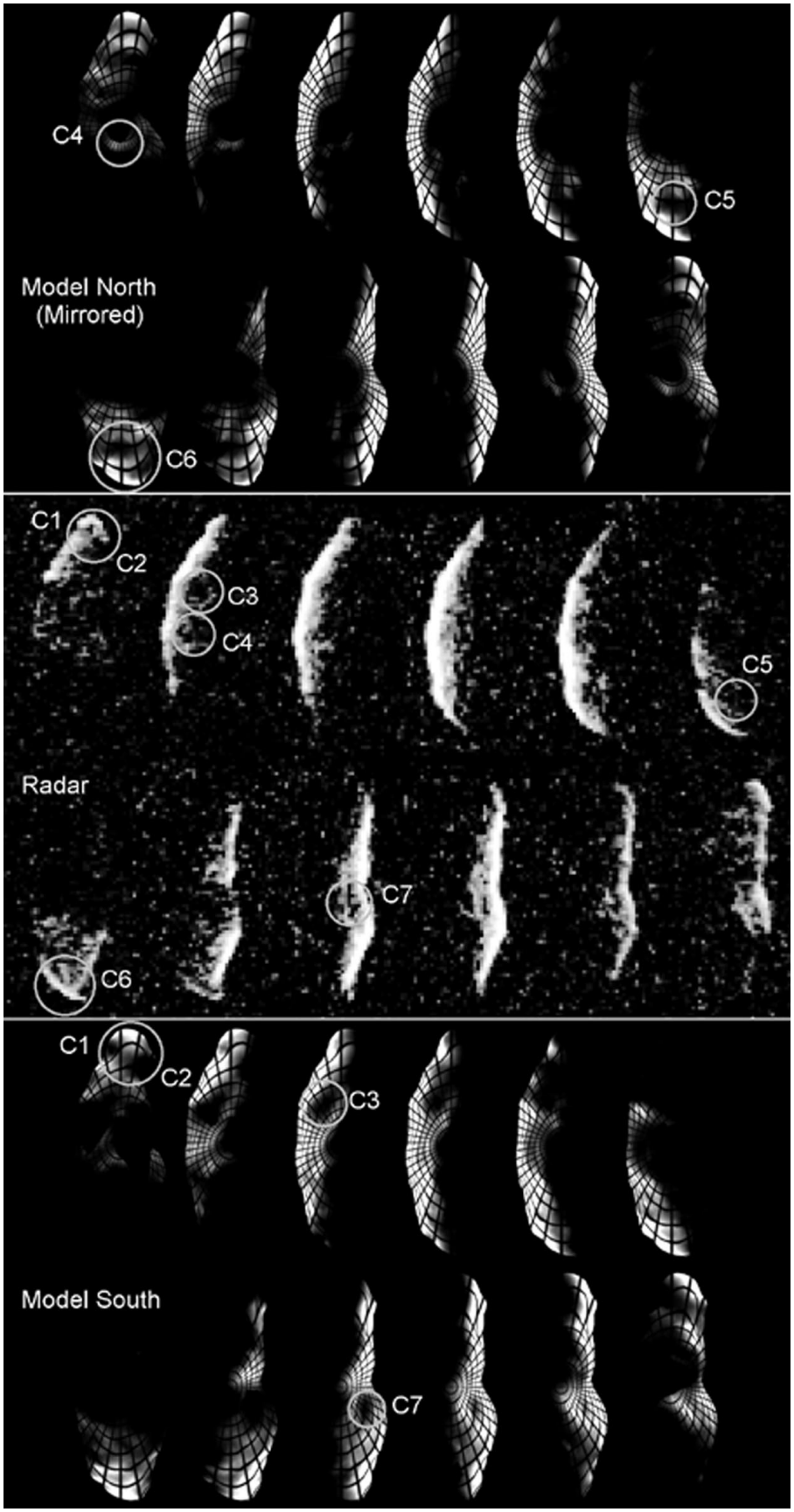

FIG. 11. Figure is divided into three sections of twelve images each. Middle section: Fig. 11 from Ostro *et al.* (1996) showing delay–Doppler images averaged over 30° rotation-phase windows. (Top) Geographos model viewed from above the north pole with longitude of the equatorial illumination varying in 30° increments. Each of the 12 images has been mirror imaged left–right to correspond to the geometry of the delay–Doppler images. (Bottom) Geographos model viewed from above the south pole with equatorial illumination varying in 30° increments.

REFERENCES

Andrews, A. K., R. S. Hudson, and D. Psaltis 1995. Optical-radar imaging of scale models for studies in asteroid astronomy. *Opt. Lett.* **20**, 2327–2329.

Asphaug, E., S. J. Ostro, R. S. Hudson, D. J. Scheeres, and W. Benz 1998. Disruption of kilometre-sized asteroids by energetic collisions. *Nature* **393**, 437–440.

Hapke, B. 1993. *Theory of Reflectance and Emittance Spectroscopy*. Cambridge Univ. Press, Cambridge, UK.

Helfenstein, P., J. Veverka, P. C. Thomas, D. P. Simonelli, K. Klaasen, T. V. Johnson, F. Fanale, J. Granahan, A. S. McEwen, M. Belton, and C. Chapman 1996. Galileo photometry of Asteroid 243 Ida. *Icarus* **120**, 48–65.

Hudson, R. S. 1993. Three-dimensional reconstruction of asteroids from radar observations. *Remote Sens. Rev.* **8**, 195–203.

Hudson, R. S., and S. J. Ostro 1994. Shape of Asteroid 4769 Castalia (1989 PB) from inversion of radar images. *Science* **263**, 904–943.

Hudson, R. S., and S. J. Ostro 1995. Shape and non-principal axis spin state of Asteroid 4179. *Science* **270**, 84–86.

Hudson, R. S., and S. J. Ostro 1998. Photometric properties of Asteroid 4179 Toutatis from lightcurves and a radar-derived physical model. *Icarus* **135**, 451–457.

Hudson, R. S., S. J. Ostro, and A. W. Harris 1997. Constraints on spin state and Hapke parameters of Asteroid 4769 Castalia using lightcurves and a radar-derived shape model. *Icarus* **130**, 165–176.

Magnusson, P., and 46 colleagues 1996. Photometric observations and modeling of Asteroid 1620 Geographos. *Icarus* **123**, 227–244.

Ostro, S. J., and 11 colleagues 1995. Extreme elongation of Asteroid 1620 Geographos from radar images. *Nature* **375**, 474–477.

Ostro, S. J., and 12 colleagues 1996. Radar observations of Asteroid 1620 Geographos. *Icarus* **121**, 46–66.

Prokof'eva, V. V., L. G. Karachkina, and V. P. Tarashchuk 1997. Investigations of oscillations in the brightness of Asteroid 1620 Geographer during its approach to the earth in 1994. *Astron. Lett.* **23**, 758–767.

Richardson, D. C., W. F. Bottke, and S. G. Love 1998. Tidal distortion and disruption of Earth-crossing Asteroids. *Icarus* **134**, 47–76.

Scheeres, D. J., S. J. Ostro, R. S. Hudson, and R. A. Werner 1996. Orbits close to Asteroid 4769 Castalia. *Icarus* **121**, 64–87.

Scheeres, D. J., S. J. Ostro, R. S. Hudson, E. M. DeJong, and S. Suzuki 1998. Dynamics of orbits close to Asteroid 4179 Toutatis. *Icarus* **132**, 53–79.

Simonelli, D. P., J. Veverka, P. C. Thomas, P. Helfenstein, and M. J. S. Belton 1995. Analysis of Gaspra lightcurves using Galileo shape and photometric models. *Icarus* **114**, 387–402.

Simonelli, D. P., J. Veverka, P. C. Thomas, P. Helfenstein, B. T. Carcich, and M. J. S. Belton 1996. Ida lightcurves: Consistency with Galileo shape and photometric models. *Icarus* **120**, 38–47.

Thomas, P. C., M. J. S. Belton, B. Carcich, C. R. Chapman, M. E. Davies, R. Sullivan, and J. Veverka 1996. The shape of Ida. *Icarus* **120**, 20–32.